Materials Today Communications 34 (2023) 104784

Contents lists available at ScienceDirect

Materials Today Communications

journal homepage: www.elsevier.com/locate/mtcomm

Microstructures in arc-welded $Al_{10}Co_{25}Cr_8Fe_{15}Ni_{36}Ti_6$ and $Al_{10.87}Co_{21.74}Cr_{21.74}Cu_{2.17}Fe_{21.74}Ni_{21.74}$ multi-principal element alloys: Comparison between experimental data and thermodynamic predictions

Jiajia Shen [a,d], Alexander C. Martin [b,d], Norbert Schell [c,d], Carolin Fink [b,*], J.P. Oliveira [a,c,d,**]

[a] Department of Mechanical and Industrial Engineering, NOVA University of Lisbon, Caparica, Portugal
[b] Department of Materials Science and Engineering, The Ohio State University, Columbus, OH, United States
[c] Helmholtz-Zentrum Hereon, Institute of Materials Physics, Max-Planck-Str. 1, Geesthacht 21502, Germany
[d] CENIMAT/I3N, Department of Materials Science, NOVA School of Science and Technology, Universidade NOVA de Lisboa, 2829-516 Caparica, Portugal

ARTICLE INFO

Keywords:
High entropy alloys
Electron microscopy
Synchrotron X-ray diffraction
Thermodynamic calculations

ABSTRACT

The development of multi-principal element alloys is currently on the rise. While there is significant fundamental work being performed to understand microstructure-property relationships, the processability of these novel alloys is yet incipient. In this work, the microstructure evolution in two arc-welded multi-principal element alloys, $Al_{10}Co_{25}Cr_8Fe_{15}Ni_{36}Ti_6$ and $Al_{10.87}Co_{21.74}Cr_{21.74}Cu_{2.17}Fe_{21.74}Ni_{21.74}$, was evaluated by electron microscopy and high energy synchrotron X-ray diffraction coupled with thermodynamic calculations. By correlating microhardness maps across the welds to results from microstructure characterization, it was possible to identify the strengthening phases across the welded materials, which can aid in fine tuning the alloy microstructure to achieve targeted strengths. Moreover, a comparison between the thermodynamically predicted microstructure evolution and that present in the welded joints was performed, highlighting the difficulty of such predictions in complex, scarcely studied multi-principal element systems.

1. Introduction

Multi-principle element alloys, also known as high entropy alloys, are recognized as novel advanced materials capable to revolutionize multiple industries owing to their extraordinary mechanical and functional properties over a wide range of conditions, these being either thermal or environmental. Discovered in 2004 independently by *Cantor* et al. [1] and *Yeh* et al. [2], these materials are typically composed of at least five principal elements. While in the first years the focus was primarily on equiatomic compositions, non-equiatomic alloys have now become predominant owing to the vast compositional space available.

As potential engineering materials to be used in structural applications, the ability to join and manufacture components from multi-principle element alloys is a major requirement. Arc-based welding processes are probably the most versatile and are used across a wide range of industries all over the world. Among the multiple arc-based welding processes available, gas tungsten arc welding (GTAW), also known as tungsten inert gas (TIG) welding, is known to ensure the best weld appearance, while at the same time is less prone to welding defects compared to other arc-based welding processes.

During GTAW, a non-consumable tungsten-based electrode is used to generate an electric arc between the electrode tip and the base material. The energy transferred to the material promotes melting of the base material (and filler material, if needed), which will then solidify as the weld bead. As a result of the weld thermal cycle three distinct regions are formed: (1) the fusion zone (FZ), where the material reached the liquid state; (2) the partially melted zone (PMZ), where the material is in the semi-solid state; and (3) the heat-affected zone (HAZ), where the temperature and permanence time are not enough for a state change (from solid to liquid as it occurs in the FZ) but rather solid-state transformations (i.e. grain growth, recrystallization and/or precipitation or dissolution of phases) occur. The rest of the joint is composed by the non-affected base material (BM).

So far, weldability studies primarily focused on single phase

* Corresponding author.
** Corresponding author at: CENIMAT/I3N, Department of Materials Science, NOVA School of Science and Technology, Universidade NOVA de Lisboa, 2829-516 Caparica, Portugal
E-mail addresses: fink.242@osu.edu (C. Fink), jp.oliveira@fct.unl.pt (J.P. Oliveira).

https://doi.org/10.1016/j.mtcomm.2022.104784
Received 20 May 2022; Received in revised form 19 October 2022; Accepted 25 October 2022
Available online 27 October 2022

Table 1
Summary of sample preparation and parameters for gas tungsten arc welding.

Alloy composition (in at. %)	Pre-weld processing	Type of weld	Weld current	Weld voltage	Travel speed
$Al_{10}Co_{25}Cr_8Fe_{15}Ni_{36}Ti_6$	Heat-treated at 1200 °C for 20 h, air-cooling	Autogenous linear weld	95 A	11 V	4.3 mm/s
$Al_{10.87}Co_{21.74}Cr_{21.74}Cu_{2.17}Fe_{21.74}Ni_{21.74}$	Hot-rolled at 800 °C to 50 % thickness reduction, then heat treated at 650 °C for 2.5 h, air-cooling	Autogenous square butt joint, two-sided	100 A	10.5 V	3.0 mm/s

equiatomic CoCrFeMnNi high entropy alloys. Even though this single-phase high entropy alloy presents excellent mechanical properties over a wide temperature range, there is not a good strength/ductility trade-off. In order to break the strength/ductility paradigm, researchers started to turn their attention to multi-principle element alloys, such as $Al_{10}Co_{25}Cr_8Fe_{15}Ni_{36}Ti_6$ and $Al_{10.87}Co_{21.74}Cr_{21.74}Cu_{2.17}Fe_{21.74}Ni_{21.74}$. However, up to now, studies on multi-principal element alloys have mainly focused on their as-cast or heat treated states. In order to make these materials potential choices for structural applications, studying different processing technologies and resulting properties is necessary. Thus, welding of these multi-principle element alloys needs to be performed to further unveil the potential of these advanced engineering materials for different applications. Both fusion [3–8] and solid-state [9–12] joining techniques have been successfully used to join some well-known multi-principle element alloys, such as CoCrFeMnNi and eutectic $AlCoCrFeNi_{2.1}$ alloys. Since there are virtually infinite possibilities in terms of alloy chemistry, it remains open which welding processes are more suitable for different multi-principle element alloy systems.

As thermodynamic databases for multi-principle element alloys become more widely available, it is possible to use CALPHAD-based (CALculation of PHAse Diagrams) thermodynamic simulation tools to predict how the weld thermal cycle affects the microstructure evolution in these complex materials. For conventional engineering alloys, such as steels (carbon or stainless) and Ni-based superalloys, these thermodynamic simulation tools are used with high accuracy to predict phase formation in the fusion zone and heat affected zone, as well as other microstructural features such as solute segregation profiles. Needless to say, that it is imperative to confirm these predictions with experimental results to assess how accurate and reliable these thermodynamic tools can be. Moreover, one can use the insights gained from experimental data to further improve the simulation strategy, as well as the existing databases.

In this work, results from weld microstructure characterization for two multi-principle element alloys, i.e. $Al_{10}Co_{25}Cr_8Fe_{15}Ni_{36}Ti_6$ and $Al_{10.87}Co_{21.74}Cr_{21.74}Cu_{2.17}Fe_{21.74}Ni_{21.74}$ (in atomic percent) were compared to predictions from CALPHAD-based thermodynamic simulations. Optical and electron microscopy, microhardness measurement and high energy synchrotron X-ray diffraction were used for characterization of the phases present in the fusion zone and heat affected zone. Relative phase fractions were determined by Rietveld refinement and correlated with the material microhardness.

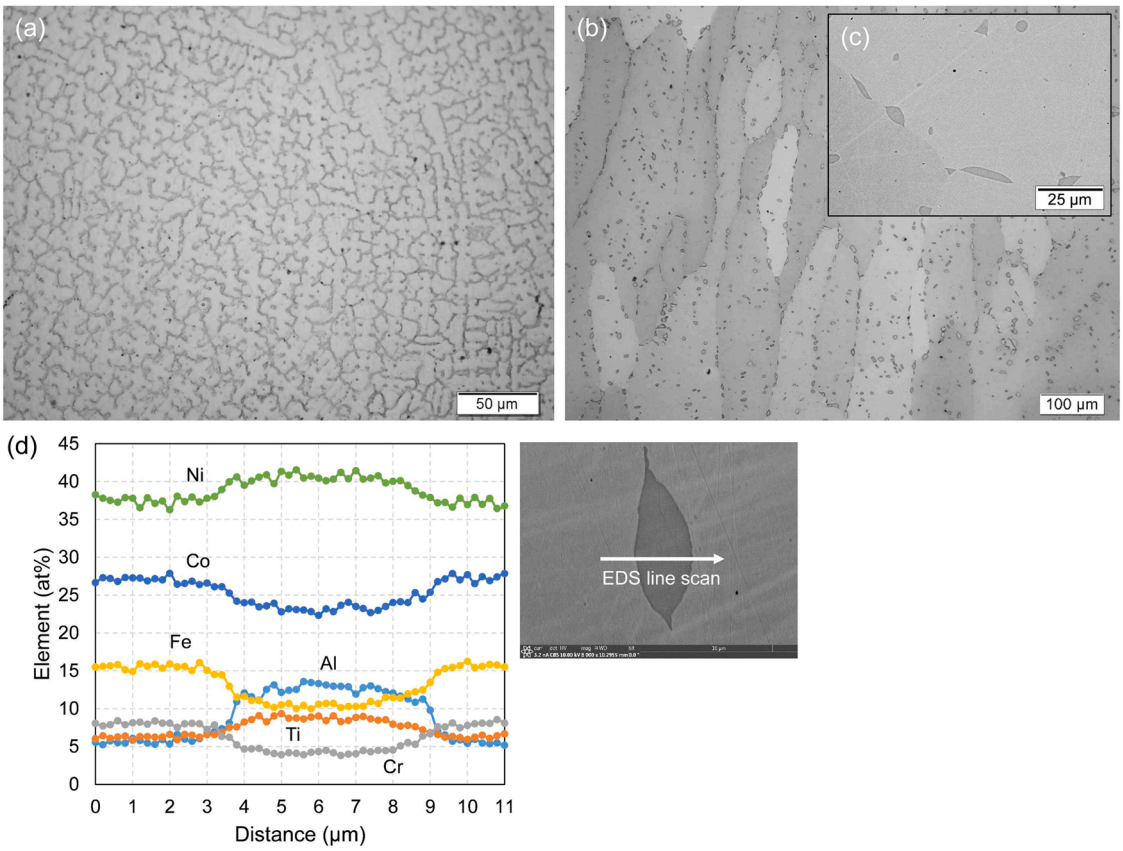

Fig. 1. Base material microstructure (etched) of $Al_{10}Co_{25}Cr_8Fe_{15}Ni_{36}Ti_6$ alloy in (a) as-cast condition; (b) after heat-treatment at 1200 °C for 20 h and subsequent air-cooling; (c) detail of heat-treated alloy showing secondary phase morphology along grain boundaries and at grain boundary triple point; and (d) semi-quantitative EDS analysis across secondary phase (location indicated in SEM-BSE image) showing enrichment in Al, Ti and Ni.

2. Materials and methods

Alloy compositions $Al_{10}Co_{25}Cr_8Fe_{15}Ni_{36}Ti_6$ and $Al_{10.87}Co_{21.74}Cr_{21.74}Cu_{2.17}Fe_{21.74}Ni_{21.74}$ (given in atomic percent, at. %) were prepared by electrode arc melting of constituent elements. Ingots (20 g) were induction melted and cast into rectangular copper molds to produce plate-shaped samples. Prior to welding, the as-cast $Al_{10}Co_{25}Cr_8Fe_{15}Ni_{36}Ti_6$ alloy was heat-treated at 1200 °C for 20 h with subsequent air-cooling. The heat treatment temperature and time were selected based on thermodynamic calculations presented in Fig. 2c. The as-cast $Al_{10.87}Co_{21.74}Cr_{21.74}Cu_{2.17}Fe_{21.74}Ni_{21.74}$ alloy was hot-rolled at 800 °C to achieve a 50 % reduction in thickness, and then subjected to a heat-treatment at 650 °C for 2.5 h. This procedure was chosen based on previous work by *Niu* et al. [13] Autogenous gas tungsten arc welding was performed on samples with dimensions of 63 × 13 × 3 mm. Details on alloy preparation and welding procedures can be found in [5]. Table 1 provides a summary of sample processing prior to welding and the welding parameters used.

Standard metallographic procedures were used to prepare weld cross-sections for light optical microscopy (LOM) and scanning electron microscopy (SEM). Polished surfaces were immersed in a molybdenum solution, containing 100 ml each of H_2O, HCl and HNO_3, and 3 g of molybdic acid (H_2MoO_4) [14] to reveal the weld microstructural features. Phase compositional data (semi-quantitative) was obtained by X-ray energy dispersive spectroscopy (XEDS) in an Apreo (Thermo Fisher Scientific Inc.) scanning electron microscope.

Synchrotron radiation allows for non-destructive characterization that can be used as a complementary method alongside with optical and electron microscopy, which are destructive characterization tools. However, unlike laboratorial X-ray sources, synchrotron X-ray radiation has higher photon flux, which enables to decrease the analysed spot size up to the nanometre scale still presenting excellent signal-to-noise ratio, which is fundamental to probe minority and nanoscale phases. Additionally, depending on the energy used, it is possible to work either in reflection or transmission mode, which enables to obtain surface or bulk information, respectively. One of the major drawbacks of a more intensive use of synchrotron radiation is the need to use large scale facilities which may be not easily accessible for researchers. Here, synchrotron X-ray diffraction was used to determine the existing phases and their volume fraction in the different regions of the weld joints. Measurements were performed at the P07 High Energy Materials Science Beamline at PETRAIII/DESY at room temperature. The diffraction experiments were performed using a beam energy of 87.1 keV. A Perkin Elmer 2D detector was used to capture the Debbye-Scherrer diffraction patterns. LaB_6 powder was used to determine the sample-to-detector distance and the instrumental peak broadening. The phase content in the base material, heat-affected zone and fusion zone was determined via Rietveld refinement using MAUD (Material Analysis Using Diffraction) software.

Microhardness mapping was performed to map the effect of the weld thermal cycle on the different weld regions. A load of 0.5 kg with a holding time of 1 s was performed with a Mitutoyo Micro Hardness Testing Machine HM-112. The distance between consecutive indentations was 250 μm in both the longitudinal and transversal directions.

Results from experimental characterization were compared to predictions from thermodynamic CALPHAD-based calculations in Thermo-Calc software (Version 2022a) using TCHEA5 database. Equilibrium step calculations, and non-equilibrium (Scheil-Gulliver) solidification calculations were performed to predict phase transformations during alloy preparation, subsequent heat-treatment of as-cast samples, and during the weld thermal cycle in the fusion zone and heat-affected zone. Calculation conditions used are detailed in [5].

Table 2
Compositions (in at. %) from Scheil calculations for $Al_{10}Co_{25}Cr_8Fe_{15}Ni_{36}Ti_6$ alloy, and comparison to measured compositions of the as-cast base material and the weld fusion zone (De: dendrite, ID: interdendritic region) measured by SEM/XEDS (semi-quantitative). Compositions taken as average of multiple measured values. Bold numbers show elements with highest interdendritic segregation. From Scheil calculations the primary solid (γ) phase (C_S) and liquid phase (C_L) compositions are reported at 0.4 and 0.78 fraction solid (f_s), respectively.

Element (at. %)	C_{nom}	Scheil calculation		As-cast base material		Weld fusion zone	
		De (C_S @ $f_s = 0.4$)	ID (C_L @ $f_s = 0.78$)	De	ID	De	ID
Al	10	9.6	11.4	9.4	**12.7**	10.5	**17.7**
Co	25	26.8	19.5	25.8	21.9	25.8	20.7
Cr	8	8.8	5.5	9.1	6.4	9.4	5.5
Fe	15	15.5	12.5	14.5	9.7	17.6	10.8
Ni	36	35.7	37.2	35.4	36.8	33.0	34.7
Ti	6	3.6	**13.9**	5.8	**12.5**	3.8	**10.8**

3. Results and discussion

3.1. Arc-welded $Al_{10}Co_{25}Cr_8Fe_{15}Ni_{36}Ti_6$ alloy

3.1.1. Base material microstructure

The dendritic solidification structure of the as-cast $Al_{10}Co_{25}Cr_8Fe_{15}Ni_{36}Ti_6$ alloy is shown in Fig. 1a. The interdendritic regions (darker etch) from solute segregation during solidification are most strongly enriched in Ti (up to 12.5 at. %), and depleted in Co, Cr and Fe as measured by SEM/XEDS analysis (results listed in Table 2). This is similar to the segregation behaviour reported by *Daoud* et al.[15], who also observed fine precipitates in the interdendritic and dendrite regions in as-cast condition. Using TEM/EDS and XRD analysis, *Manzoni* et al. [16] later identified a Co-Cr-Fe rich γ (fcc) matrix with small γ' (Ni-Al-Ti) precipitates in the dendrites, and a bcc Heusler (Al-Ni)-type matrix with needle-shaped η (Ni-Ti) phase in the interdendritic regions.

Predictions from non-equilibrium (Scheil-Gulliver) calculations indicate that solidification of the $Al_{10}Co_{25}Cr_8Fe_{15}Ni_{36}Ti_6$ alloy starts with the formation of primary γ dendrites with disordered fcc structure followed by Heusler-type and Ni_3Ti (η) interdendritic phases (Fig. 2a). Strong partitioning of Ti to the interdendritic regions is predicted, as shown in Fig. 2b and Table 2. Phase compositions from Scheil calculations are reported in Table 3. Results from these Scheil calculations are in good agreement with results from experimental characterization by *Manzoni* et al. [16], both in terms of phase formation and composition. Formation of γ' phase is not predicted on solidification as expected. Equilibrium calculations using the nominal alloy composition (presented in Fig. 2c) show that γ' is stable at elevated temperatures, indicating that γ' precipitates formed during cooling of the as-cast alloy as reported by *Manzoni* et al. [16] and as known for many superalloys.

Manzoni et al. [16] homogenized the as-cast alloy at 1220 °C for 20 h with subsequent furnace-cooling. This resulted in the complete dissolution of the interdendritic phases, and left a two-phase γ-γ' microstructure. The γ' phase formed under slow cooling conditions in the furnace [16]. In this work, the same heat treatment on the as-cast alloy did not result in a homogenized microstructure. In fact, equilibrium calculations (Fig. 2c) predict liquid to be present around 1200 °C for the nominal alloy composition. Therefore, the heat treatment temperature for the as-cast alloy was lowered in this work to 1200 °C for 20 h with subsequent air-cooling. Again, this did not result in a complete dissolution of the interdendritic phase. Discrete second phase particles were observed along grain boundaries, and intragranular in locations of former interdendritic regions (Fig. 1b). Semi-quantitative SEM/XEDS analysis showed this phase to be significantly enriched in Al, Ti and Ni (Fig. 1d), which supports the hypothesis that this phase formed from the interdendritic composition. In addition, its spread-out morphology along grain boundaries and at grain boundary triple points was noted, as

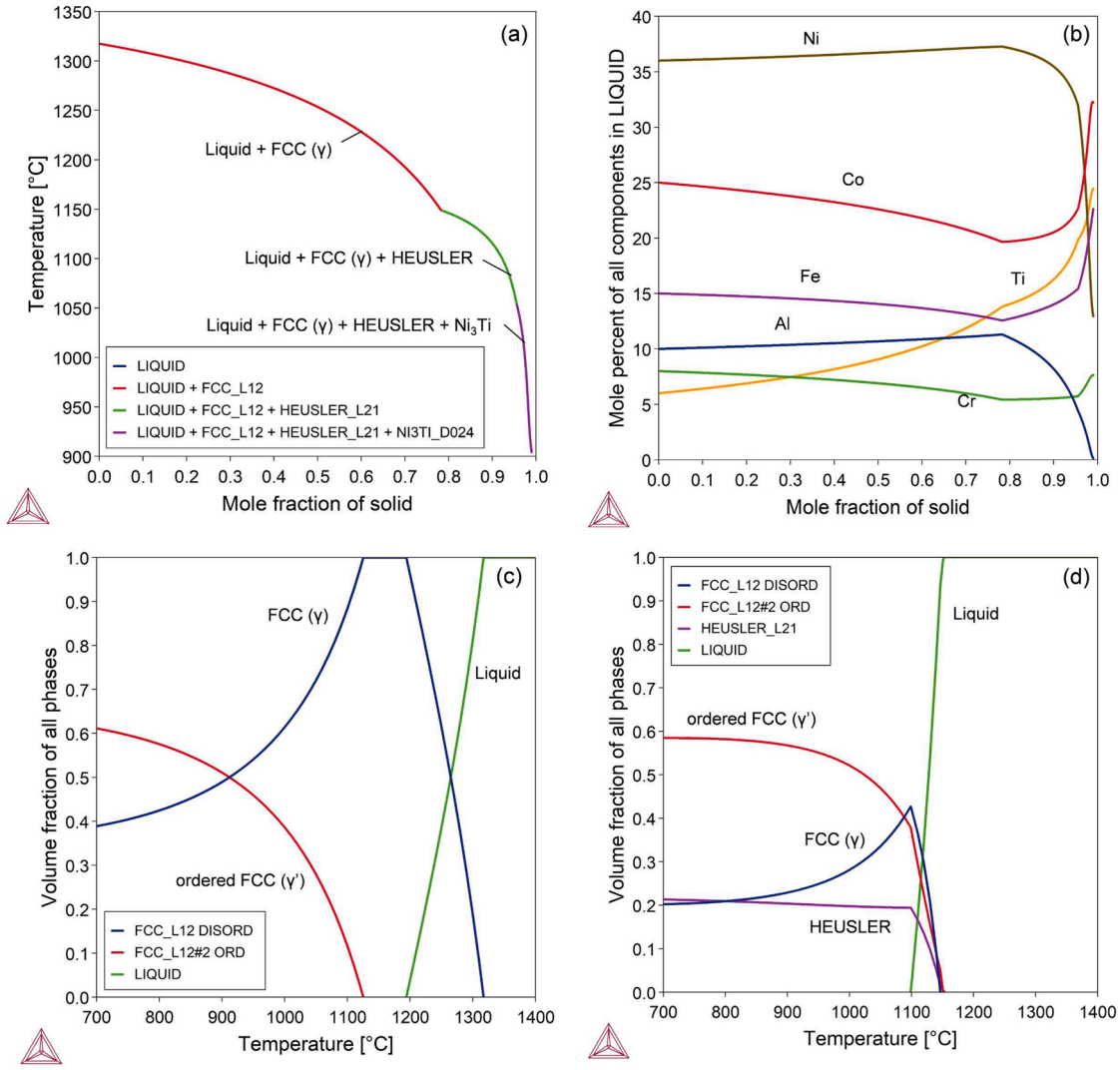

Fig. 2. Results from thermodynamic calculations for $Al_{10}Co_{25}Cr_8Fe_{15}Ni_{36}Ti_6$ alloy (nominal alloy composition): (a) Scheil solidification predicting fcc (γ) dendrites, and Heusler-type and Ni_3Ti (η) interdendritic phase; (b) composition of liquid phase obtained from Scheil calculations; (c) equilibrium calculation on nominal alloy composition with γ' phase being stable at elevated temperatures; and (d) equilibrium calculation on interdendritic composition obtained from Scheil calculations (Table 2) showing liquid phase at 1100 °C.

Table 3
Predicted phase compositions (in at%) from Scheil calculations on $Al_{10}Co_{25}Cr_8Fe_{15}Ni_{36}Ti_6$ alloy. Bold numbers show elements with the highest percentage.

Phase	Composition taken at fraction solid (f_s)	Composition (at%)						Mole percent of solid phase
		Al	Co	Cr	Fe	Ni	Ti	
fcc (γ)	0.4	9.6	**26.8**	8.8	15.5	**35.7**	3.6	~94
Heusler	0.88	**26.1**	7.6	–	–	**44.9**	**21.4**	~5
Ni_3Ti (η)	0.97	1.4	7.8	0.7	2.8	**63.7**	**23.6**	~1

shown in Fig. 1c. This indicates that liquation of the interdendritic regions might have occurred locally during heat treatment, and facilitated spreading of liquid along the grain boundaries. Equilibrium calculations using the interdendritic composition from Scheil-Gulliver simulation (listed in Table 2) predict liquid just below 1100 °C (Fig. 2d), which further supports this hypothesis. The difference in the alloy's reaction to the homogenization heat treatment in this work as compared to the work by *Manzoni* et al. [16] may be explained by a difference in the heating rate up to the heat treatment temperature. Slower heating due to larger sample size, as in the work by *Manzoni* et al. [16], may have allowed for sufficient diffusion between dendritic and interdendritic regions before the peak temperature was reached. This may have avoided liquation and resulted in the complete dissolution of the interdendritic phase during heat treatment.

A representative synchrotron X-ray diffraction pattern from the $Al_{10}Co_{25}Cr_8Fe_{15}Ni_{36}Ti_6$ alloy in the as-cast and heat-treated (1200 °C for 20 h) condition is depicted in Fig. 3a. Only diffraction peaks corresponding to fcc phase (named FCC#1) were observed. The existence of multiple fcc phases may not be neglected, since it is possible that these would have very similar lattice parameters. *Manzoni* et al.[17]showed γ and γ' phases in the as-cast alloy indistinguishable from one another in conventional X-ray diffraction patterns. This is also known to occur in Ni-base superalloys [18]. The results from synchrotron X-ray diffraction and semi-quantitative SEM/XEDS (Fig. 1d) indicate that the second

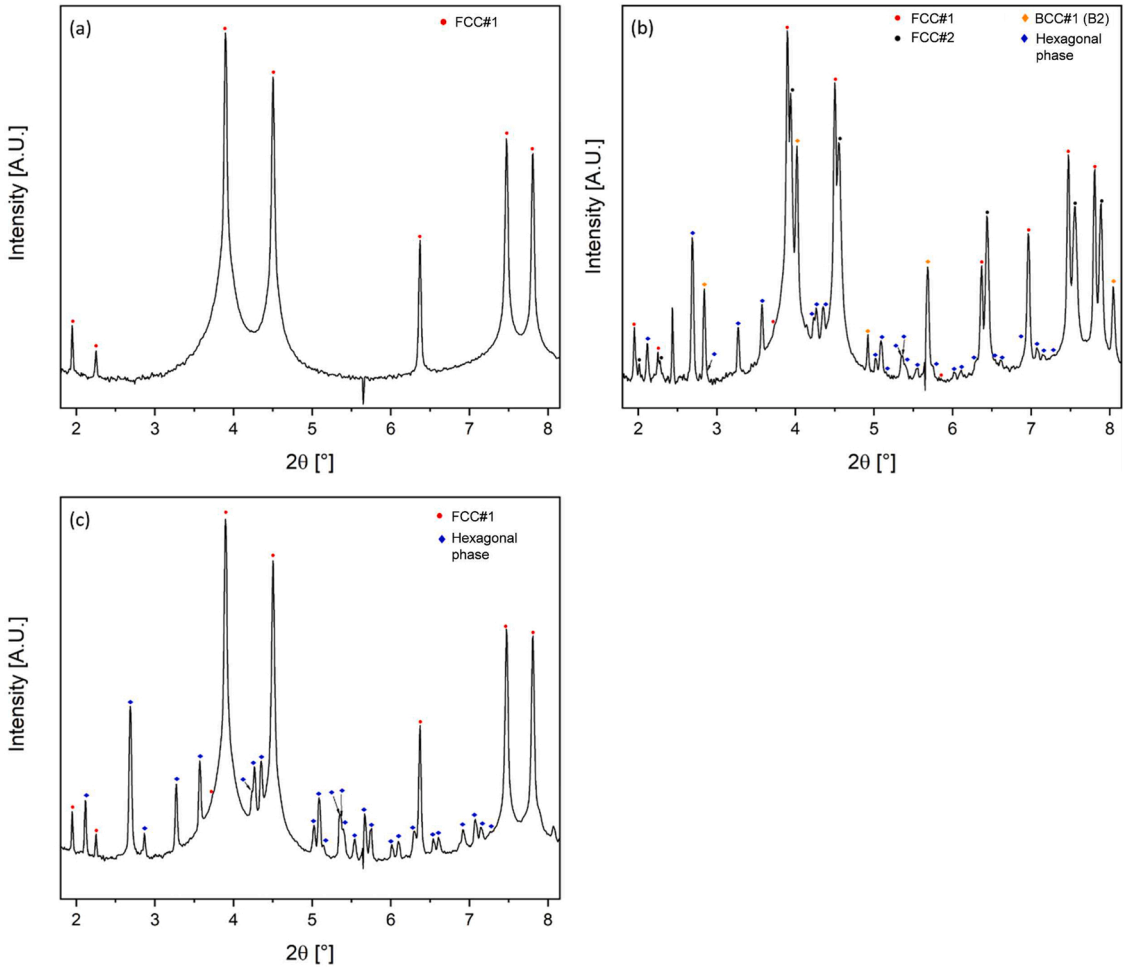

Fig. 3. Representative X-ray diffraction patterns of $Al_{10}Co_{25}Cr_8Fe_{15}Ni_{36}Ti_6$ alloy in (a) the heat-treated (1200 °C for 20 h) base material condition, and from (b) the fusion zone and (c) the heat-affected zone of the gas tungsten arc welded alloy.

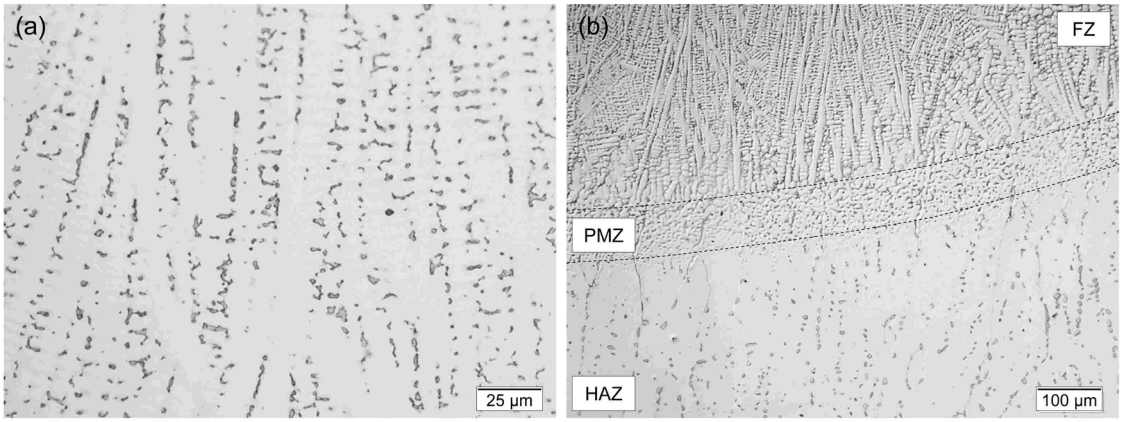

Fig. 4. Weld microstructures (etched) of $Al_{10}Co_{25}Cr_8Fe_{15}Ni_{36}Ti_6$ alloy: (a) fusion zone and (b) transition region across the fusion boundary into the partially melted zone (PMZ) and heat-affected zone (HAZ).

phase in the as-cast and heat treated base material (Fig. 1b) is γ' phase (Ni-Al-Ti rich) that formed from the interdendritic composition.

3.1.2. *Fusion zone microstructure*

The fusion zone microstructure of the gas tungsten arc welded $Al_{10}Co_{25}Cr_8Fe_{15}Ni_{36}Ti_6$ alloy consists of distinct dendritic and interdendritic regions (Fig. 4a). The segregated solidification structure and elemental distribution in the dendrite core versus the interdendritic regions are very similar to what is seen in the as-cast base material (Table 2). Strong partitioning of Ti and Al was observed. Cellular-dendritic and columnar-dendritic are the primary solidification growth modes throughout the fusion zone. The higher solidification rate of the weld as compared to the as-cast alloy results in a smaller solidification length scale for the fusion zone microstructure.

Table 4
Refined lattice parameters from base material (BM), fusion zone (FZ) and heat-affected zone (HAZ) of gas tungsten arc welded $Al_{10}Co_{25}Cr_8Fe_{15}Ni_{36}Ti_6$ as obtained from high energy synchrotron X-ray diffraction.

Region	FCC#1	FCC#2	BCC#1 (B2)	Hexagonal phase
BM	a = b = c= 0.36226 nm α = β = γ = 90°	–	–	–
FZ	a = b = c= 0.36226 nm α = β = γ = 90°	a = b = c= 0.35866 nm α = β = γ = 90°	a = b = c= 0.28699 nm α = β = γ = 90°	a = b = 0.497964 nm, c = 0.85593 nm α = β = 90°, γ = 120°
HAZ	a = b = c= 0.36224 nm α = β = γ = 90°	–	–	a = b = 0.498141 nm, c = 0.85589 nm α = β = 90°, γ = 120°

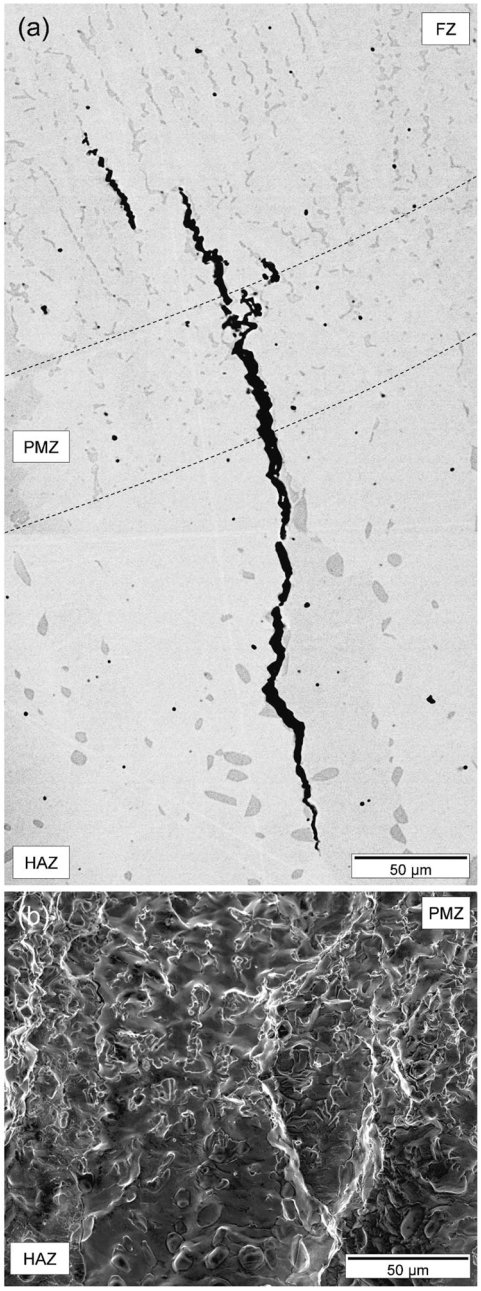

Fig. 5. SEM images of liquation cracking in the gas tungsten arc welded $Al_{10}Co_{25}Cr_8Fe_{15}Ni_{36}Ti_6$ alloy: (a) cracking (shown in cross-section) is due to liquid film formation in the partially melted zone (PMZ), i.e. the high temperature heat-affected zone adjacent to the fusion line; (b) fracture surface shows evidence of extensive liquid film formation.

Fig. 3b shows a representative diffraction pattern from the fusion zone. Two fcc phases (named FCC#1 and FCC#2), one bcc (B2) phase (BCC#1) and one hexagonal phase were observed. It should be noted that some second order harmonics, which originate from the extremely high energy of the synchrotron X-ray beam were observed for lower 2θ angles. These second order reflections were in fact a duplication of the FCC#1 diffraction peaks located at 2θ = 3.90° and 4.50°. Volume fraction calculations of the phases present in the fusion zone yielded ~38 % for FCC#1, ~30 % for FCC#2, ~19 % for BCC#1 and ~13 % for the hexagonal phase. The lattice parameters for all phases, as obtained by Rietveld refinement, are listed in Table 4. The lattice parameters of FCC#1 (a = 0.36226 nm) and FCC#2 (a = 0.35866 nm) are close to those obtained for γ and γ' (Ni-Co-Fe)$_3$(Al-Ti-Cr) phases by *Manzoni* et al. [16] when analysing the as-cast $Al_{10}Co_{25}Cr_8Fe_{15}Ni_{36}Ti_6$ alloy. TEM/EDS characterization determined the chemical composition of the γ' phase to be Al-Ni-Ti-rich. SEM imaging in this work was not able to resolve γ' in the γ dendrites of the fusion zone microstructure. Much smaller γ' precipitates would be expected in the fusion zone microstructure as compared to the as-cast alloy in [16] due to the faster cooling rate of the weld. The bcc (B2) phase (BCC#1) in the diffraction pattern in Fig. 3b is believed to correspond to what has been reported as bcc Heusler (Al-Ni)-type phase by *Manzoni* et al. [16]. In a similar alloy composition, $AlCoCrFeNiTi_{0.5}$, *Moravcik* et al. [19] obtained a lattice parameter for bcc (B2) Al-Ni-rich phase that is close to what is reported here (a = 0.28699 nm). The lattice parameters of the hexagonal phase observed in this work (a = b = 0.49796 nm and c = 0.85593 nm) are again in good agreement to those obtained by *Manzoni* et al. [16] for interdendritic η (Ni_3Ti)-phase.

As discussed earlier, non-equilibrium (Scheil) solidification calculations (Fig. 2a) predict fcc γ dendrites to form, followed by Heusler-type and Ni_3Ti (η) phases at the end of weld solidification. This is in good agreement with the phases experimentally observed from synchrotron X-ray diffraction in the fusion zone microstructure in this work. The second fcc phase in the diffraction pattern (FCC#2) is believed to be γ' (Ni-Co-Fe)$_3$(Al-Ti-Cr) phase, which formed during cooling of the solidified weld metal.

3.1.3. *Heat-affected zone microstructure*

The heat-affected zone of the gas tungsten arc welded $Al_{10}Co_{25}Cr_8Fe_{15}Ni_{36}Ti_6$ alloy consists of two distinct regions. A partially melted zone (PMZ) is observed immediately adjacent to the fusion line, as shown in Fig. 4b. The PMZ is about 100–150 μm wide. This region of the heat-affected zone experiences the highest peak temperatures during the weld thermal cycle. As a result, extensive liquation occurs along grain boundaries and intragranular regions in the base material microstructure (Fig. 4b). Thermodynamic calculations (shown earlier in Fig. 2d), indicate that the peak temperatures for liquation to occur in the partially melted zone are around 1100 °C and above. These liquid films spread along grain boundaries and contribute to the formation of liquation cracking if sufficient localized strain and stress act to pull them apart. Stress and strain fields are generated around the moving weld pool due to shrinkage of the solidifying molten pool, and thermal contraction and restraint of the surrounding base material. Fig. 5 shows an example of a liquating crack that originated from liquid films generated in the partially melted zone and propagated along grain boundaries in the

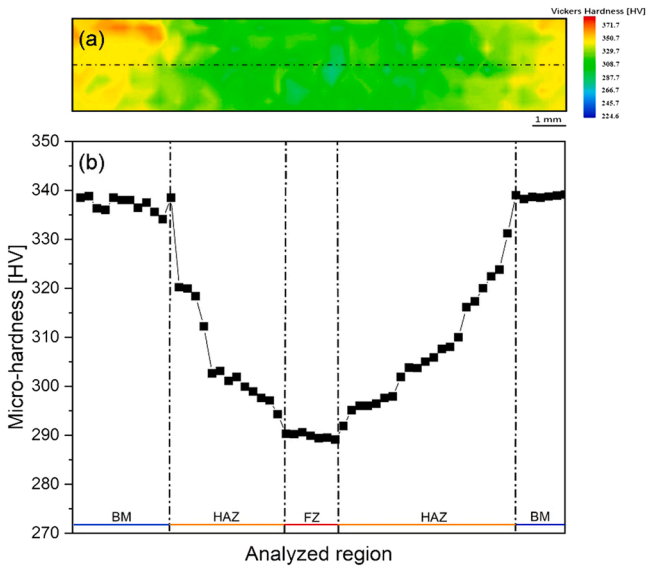

Fig. 6. (a) Microhardness map across the gas tungsten arc welded $Al_{10}Co_{25}Cr_8Fe_{15}Ni_{36}Ti_6$ alloy with (b) a specific hardness distribution across the different weld regions (black dashed line in hardness map).

heat-affected zone and into the fusion zone.

In the heat-affected zone only diffraction peaks of fcc phase and hexagonal phase were observed by synchrotron X-ray diffraction (Fig. 3c). As previously discussed for the XRD data obtained from the base material, the presence of two fcc phases (γ and γ') may be disguised due to the very similar lattice parameters. The calculated volume fraction for FCC#1 and hexagonal phase was 77 % and 23 %, respectively. Interestingly hexagonal phase was observed in the heat-affected zone, despite not being present in the heat-treated base material. This may be related to the high temperature exposure in the heat-affected zone and phase transformation kinetics that need to be further explored in this alloy system. The physical metallurgy of multi-principal elements is often different from that of conventional alloys [20]. The previous base material condition and thermal cycle experienced by the material can lead to the development of unexpected phases, as the hexagonal phase detected in this work. So far, the mechanism for the formation of this phase is unclear and future work will be dedicated to further explore the formation of this phase under different thermo-mechanical conditions using in-situ synchrotron X-ray diffraction measurements.

3.1.4. Microhardness

A microhardness map of the gas tungsten arc welded $Al_{10}Co_{25}Cr_8Fe_{15}Ni_{36}Ti_6$ alloy and a line scan obtained across the weld at mid-height (black dashed line) are shown in Fig. 6. The average hardness of the base material, the heat-affected zone and the fusion zone was ~338 HV, ~308 HV and ~290 HV, respectively. The weld thermal cycle and the resulting microstructural changes have an evident impact on the material hardness. The hardness drops in the heat-affected zone as compared to the heat-treated base material. This may in fact indicate a dissolution of γ' phase upon high temperature exposure in the heat-affected zone. In the fusion zone, the hardness is at its minimum. However, the multiphase microstructure in the fusion zone of $Al_{10}Co_{25}Cr_8Fe_{15}Ni_{36}Ti_6$ alloy still yields a higher hardness than what is seen in other well-known multiple principle element entropy alloys, such as the equiatomic CoCrFeMnNi (≈ 150 HV) [7].

3.2. Arc-welded $Al_{10.87}Co_{21.74}Cr_{21.74}Cu_{2.17}Fe_{21.74}Ni_{21.74}$ alloy

3.2.1. Base material microstructure

The base material microstructure of the $Al_{10.87}Co_{21.74}Cr_{21.74}Cu_{2.17}Fe_{21.74}Ni_{21.74}$ alloy in the hot-rolled and heat-treated condition is shown in Fig. 7. Previous work by the authors [5] reported highly deformed Co-Cr-Fe rich γ (fcc) dendrites and interdendritic regions with bcc crystalline structure. The hardness was measured at 429 HV, which was a significant increase as compared to the as-cast condition (208 HV) and was attributed to an increase in dislocation density from forming and strong subsequent precipitation of nano-sized bcc (B2) phase [5,13]. Predictions from equilibrium calculations, shown in Fig. 8a, are in good agreement, indicating the ordered bcc (B2) phase to be stable over a large temperature range in this alloy. Fig. 8a also shows that no single-phase region exists below the melting range for this alloy, which would typically be desirable to perform homogenization heat treatments. It should be mentioned that the thermodynamic calculations detailed in Fig. 8 are similar to those reported in [5]. The reason for the inclusion of these calculations in the present paper is related to the development of new databases for multicomponent alloys which are expected to be more accurate than previous version. In fact, between reference [5] and the TCHEA database of ThermoCalc was updated twice (from TCHEA3 to TCHEA5), with improved thermodynamic information for multicomponent alloys.

Fig. 9a shows a representative synchrotron X-ray diffraction pattern from the $Al_{10.87}Co_{21.74}Cr_{21.74}Cu_{2.17}Fe_{21.74}Ni_{21.74}$ alloy in the hot-rolled and heat-treated condition. Similar to the $Al_{10}Co_{25}Cr_8Fe_{15}Ni_{36}Ti_6$ alloy base material previously discussed (Section 3.1), only diffraction peaks corresponding to fcc phase were observed. This is contrary to previously performed conventional X-ray diffraction data, which had shown an additional disordered bcc phase present in the heat-treated condition [5]. Nano-sized bcc (B2) phase [13] was not observed using conventional X-ray diffraction [5], but also did not show in the high energy

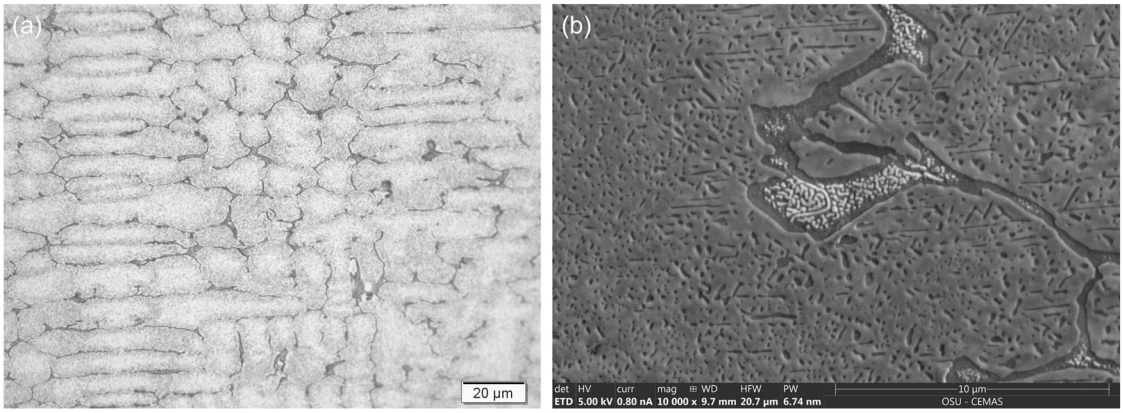

Fig. 7. Base material microstructure of $Al_{10.87}Co_{21.74}Cr_{21.74}Cu_{2.17}Fe_{21.74}Ni_{21.74}$ alloy after hot-rolling at 800 °C to 50 % thickness reduction and subsequent heat-treatment at 650 °C for 2.5 h with air-cooling: (a) Light optical micrograph (etched); and (b) higher magnification SEM image.

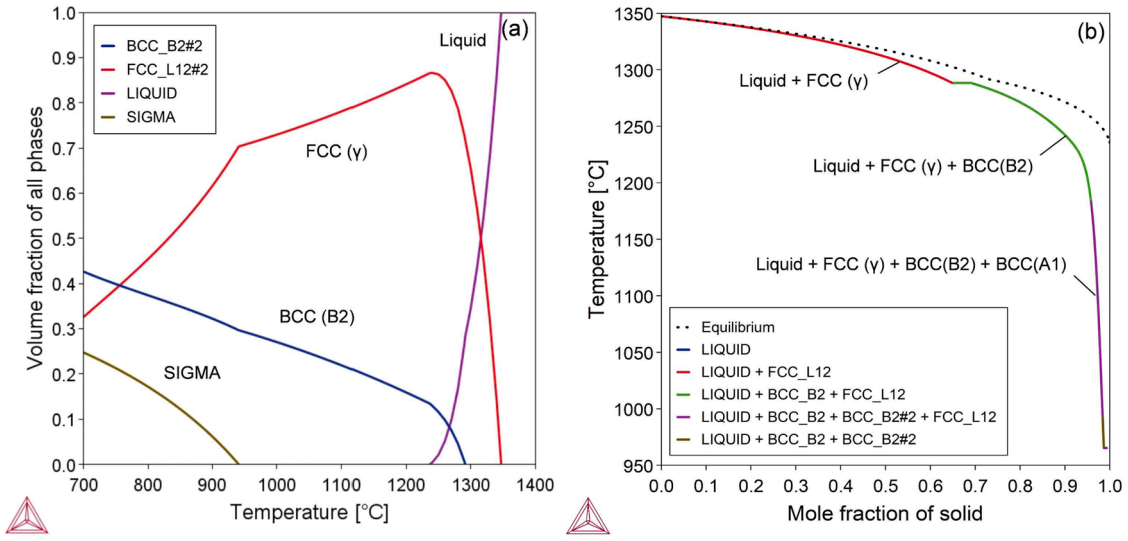

Fig. 8. Results from thermodynamic calculations for $Al_{10.87}Co_{21.74}Cr_{21.74}Cu_{2.17}Fe_{21.74}Ni_{21.74}$ alloy (nominal alloy composition): (a) Equilibrium calculation with fcc (γ) and bcc (B2) as stable phases close to the melting temperature; and Sigma phase stable at lower temperatures; and (b) Scheil solidification calculation predicting fcc (γ) dendrites, and bcc (B2) and bcc (A1) interdendritic phase.

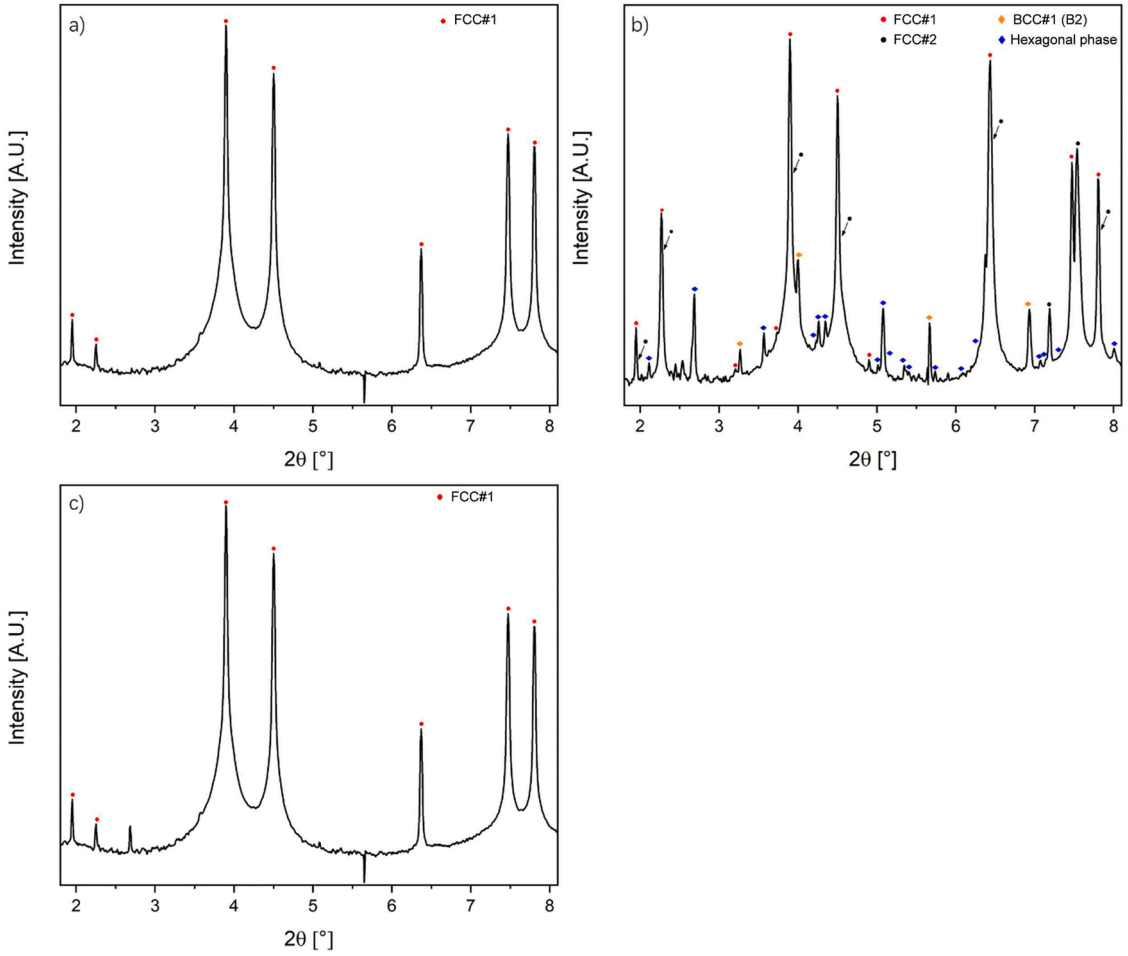

Fig. 9. Representative X-ray diffraction pattern of $Al_{10.87}Co_{21.74}Cr_{21.74}Cu_{2.17}Fe_{21.74}Ni_{21.74}$ alloy in (a) the hot-rolled and heat treated base material condition, and from (b) the fusion zone and (c) the heat-affected zone of the gas tungsten arc welded alloy.

synchrotron X-ray diffraction patterns obtained in this work.

3.2.2. *Fusion Zone Microstructure*

The fusion zone microstructure of the gas tungsten arc welded $Al_{10.87}Co_{21.74}Cr_{21.74}Cu_{2.17}Fe_{21.74}Ni_{21.74}$ alloy consists of distinct

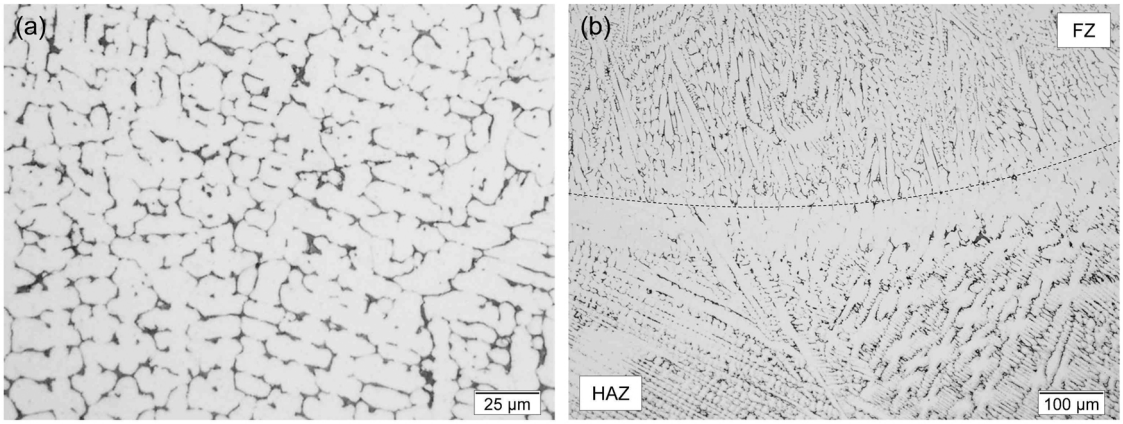

Fig. 10. : Weld microstructures (etched) of $Al_{10.87}Co_{21.74}Cr_{21.74}Cu_{2.17}Fe_{21.74}Ni_{21.74}$ alloy: (a) fusion zone and (b) transition region across the fusion boundary into the heat-affected zone (HAZ).

Table 5
Measured compositions (in at%) from the fusion zone of gas tungsten arc welded $Al_{10.87}Co_{21.74}Cr_{21.74}Cu_{2.17}Fe_{21.74}Ni_{21.74}$ alloy (De: dendrite, ID: interdendritic region) measured by SEM/XEDS (semi-quantitative), and comparison to predicted compositions from Scheil calculation. Compositions taken as average of multiple measured values. Bold numbers show elements with highest interdendritic segregation. From Scheil calculations the primary solid (γ) phase (C_S) and liquid phase (C_L) compositions are reported at 0.4 and 0.65 fraction solid (f_s), respectively.

Element (at. %)	C_{nom}	Weld fusion zone		Scheil calculation	
		De	ID	De (C_S @ f_s = 0.4)	ID (C_L @ f_s = 0.65)
Al	10.87	11.1	**20.5**	4.3	**8.2**
Co	21.74	20.7	15.7	26.3	19.4
Cr	21.74	23.8	22.8	22.6	18.6
Cu	2.17	2.6	3.7	0.9	**6.2**
Fe	21.74	21.2	15.4	23.6	20.8
Ni	21.74	20.6	21.6	22.3	26.8

dendritic and interdendritic regions, as seen in Fig. 10a. The grain structure near the fusion line is dominated by epitaxial growth. Cellular solidification close to the fusion line quickly breaks down into cellular-dendritic and columnar-dendritic solidification mode throughout most of the fusion zone. Semi-quantitative compositional analysis (SEM-XEDS) shows a slight enrichment in Cr, but overall, the dendrite core composition is similar to the nominal alloy composition (Table 5). The interdendritic regions are very highly enriched in Al, and depleted in Co and Fe. Copper was found to be slightly enriched in the interdendritic regions (3.7 at%). For alloy compositions with a higher nominal Cu content (> 5.6 at%) strong partitioning has been reported to result in the formation of a Cu-rich liquid phase during weld solidification that promotes solidification cracking in the fusion zone due to its low effective solidus temperature [21].

According to the synchrotron X-ray diffraction pattern of the fusion zone (Fig. 9b) a multi-phase microstructure composed of two ordered fcc phases (named FCC#1 and FCC#2), one bcc (B2) phase (BCC#1) and one hexagonal phase is present. Volume fraction calculations of the phases present in the fusion zone yielded ~46 % for FCC#1, ~23 % for FCC#2, ~18 % for BCC#1 and ~13 % for the hexagonal phase, respectively. The lattice parameters for all phases, as obtained by Rietveld refinement, are listed in Table 7. In the as-cast equiatomic alloy composition, AlCoCrCuFeNi, *Singh* et al. [22] obtained a lattice parameter for bcc (B2) Al-Ni-rich phase that is close to what is reported here (2.88 ± 0.02 Å). The results for this multi-phase region are indeed very similar to the fusion zone microstructure that composes the $Al_{10}Co_{25}Cr_8Fe_{15}Ni_{36}Ti_6$ welded joint. The second fcc phase may be a metastable Cu-rich phase as previously shown in [23]. The hexagonal phase that is observed is believed to be Cr-Fe-rich sigma (σ) phase [24].

Predictions from Scheil calculations indicate that the

Table 6
Predicted phase compositions (in at%) from Scheil calculations on $Al_{10.87}Co_{21.74}Cr_{21.74}Cu_{2.17}Fe_{21.74}Ni_{21.74}$ alloy. Bold numbers show elements with the highest percentage.

Phase	Composition taken at fraction solid (f_s)	Composition (at%)						Mole percent of solid phase
		Al	Co	Cr	Cu	Fe	Ni	
fcc (γ)	0.4	4.3	**26.3**	22.6	0.9	**23.6**	22.3	~86
bcc (B2)	0.85	**26.2**	17.6	8.7	3.3	15.8	**28.4**	~13
bcc (A1)	0.98	1.5	1.6	**65.5**	–	**25**	**6.5**	< 1

Table 7
Refined lattice parameters from base material (BM), fusion zone (FZ) and heat-affected zone (HAZ) of gas tungsten arc welded $Al_{10.87}Co_{21.74}Cr_{21.74}Cu_{2.17}Fe_{21.74}Ni_{21.74}$ as obtained from high energy synchrotron X-ray diffraction.

Region	FCC#1	FCC#2	BCC#1 (B2)	Hexagonal phase
BM	a = b = c= 0.36231 nm α = β = γ = 90°	–	–	–
FZ	a = b = c= 0.36225 nm α = β = γ = 90°	a = b = c= 0.35896 nm α = β = γ = 90°	a = b = c= 0.28849 nm α = β = γ = 90°	a = b = 0.506093 nm, c = 0.87934 nm α = β = 90°, γ = 120°
HAZ	a = b = c= 0.36230 nm α = β = γ = 90°	–	–	–

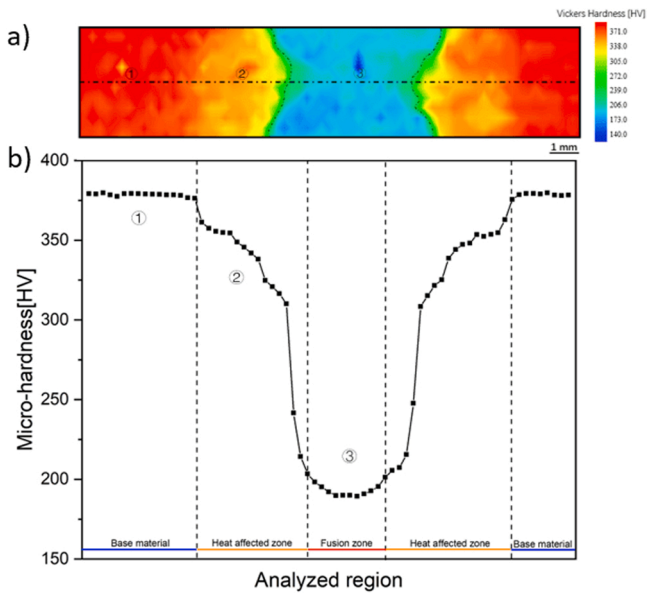

Fig. 11. a) Microhardness map across the gas tungsten arc welded $Al_{10.87}Co_{21.74}Cr_{21.74}Cu_{2.17}Fe_{21.74}Ni_{21.74}$ alloy with (b) a specific hardness distribution across the different weld regions (black dashed line in hardness map).

$Al_{10.87}Co_{21.74}Cr_{21.74}Cu_{2.17}Fe_{21.74}Ni_{21.74}$ alloy solidifies primarily as fcc (γ) dendrites with a small amount of Al-Ni-rich ordered bcc (B2) phase that forms as solidification proceeds (Fig. 8b). Strong partitioning of Al and Cu to the interdendritic regions is predicted (Table 5). During the final stages of solidification, a Cr-Fe-rich disordered bcc (A1) phase is predicted to form, however the final amount of this phase is less than one mole percent (Table 6). The phase compositions and crystal structures are in overall good agreement with characterization results reported previously in [5] and in this study. The predicted Cr-Fe-rich bcc phase may in fact be hexagonal sigma phase. No second fcc phase is predicted to form on Scheil solidification.

3.2.3. *Heat-affected zone microstructure*

In the high temperature heat-affected zone (HAZ) of the reheated base material partial dissolution of the interdendritic phase was observed over an approximately 100 μm wide region immediately adjacent to the fusion line, as seen in Fig. 10**b**. The thermodynamic calculations shown in Fig. 8**a** do not show a single-phase region below the melting range of the alloy, but fcc (γ) is the primary phase at temperatures just below the melting temperature. According to the synchrotron X-ray diffraction pattern of the heat affected zone (Fig. 9**c**) only one fcc phase (FCC#1) is indexed. This is similar to what was previously reported for the heat affected zone of the $Al_{10}Co_{25}Cr_8Fe_{15}Ni_{36}Ti_6$ joint.

3.2.4. *Microhardness*

To further evaluate the impact of the weld thermal cycle on the welded $Al_{10.87}Co_{21.74}Cr_{21.74}Cu_{2.17}Fe_{21.74}Ni_{21.74}$ alloy, microhardness mapping was performed. Results are detailed in Fig. 11. The highest hardness (~376 HV) is found in the hot rolled and heat treated base material. Upon entering in the heat affected zone a slight hardness decrease to ~350 HV is observed. Closer towards the fusion line, a more significant hardness drop to ~300 HV is observed in the heat affected zone. This is also due to the reheating induced by the heat source promoting material softening, thus decreasing the strain hardening from hot rolling of the base material prior to welding. In this region of the material only one fcc phase was observed using X-ray diffraction. The lowest hardness is found in the fusion zone, where a multi-phase microstructure exists. The hardness is lower as compared to the fusion zone of the $Al_{10}Co_{25}Cr_8Fe_{15}Ni_{36}Ti_6$ alloy, but still above that of conventional and well-known high-entropy alloys, such as equiatomic CoCrFeMnNi [7].

4. Conclusions

In this work, two multi-principal elemental alloys, $Al_{10}Co_{25}Cr_8Fe_{15}Ni_{36}Ti_6$ and $Al_{10.87}Co_{21.74}Cr_{21.74}Cu_{2.17}Fe_{21.74}Ni_{21.74}$, were welded using gas tungsten arc welding. By combining results from thermodynamic calculations and microstructure characterization, the microstructure evolution across the welded joints was rationalized. Moreover, hardness mapping of the welded joints allowed to understand the role of the phases present on the mechanical properties across the welded joint. The following major conclusions were drawn:

- In the $Al_{10}Co_{25}Cr_8Fe_{15}Ni_{36}Ti_6$ and $Al_{10.87}Co_{21.74}Cr_{21.74}Cu_{2.17}Fe_{21.74}Ni_{21.74}$ arc welded joints, the heat affected zone and fusion zone possessed different microstructure compared to the original base materials, this being due to the effect of weld thermal cycle.
- Overall, a good agreement was obtained between predictions from equilibrium and non-equilibrium solidification calculations and results from microstructure characterization was obtained. In some instance differences between predicted and experimentally observed phases were noted. This is attributed to the complexity of the alloy systems investigated in this work. Thus, there is a need for a continued development of thermodynamic databases focused on non-conventional multicomponent alloy systems further increase accuracy of predictions.
- By impacting the microstructure evolution, the weld thermal cycle greatly influenced the joints microhardness. The microhardness of both $Al_{10}Co_{25}Cr_8Fe_{15}Ni_{36}Ti_6$ and $Al_{10.87}Co_{21.74}Cr_{21.74}Cu_{2.17}Fe_{21.74}Ni_{21.74}$ arc welded joints had a decrease of hardness in the heat affected zone relatively to the base material. For the former alloy, this occurs due to the dissolution of γ' phase upon the high temperature exposure in the heat-affected zone, while for the latter this is related to the reheating induced by the heat source promoting the released of the dislocations and strain from the base material, thus inducing the material softening in the heat affected zone. In the fusion zone, the hardness in both welded joints exhibited the lowest value, despite being significantly higher than that obtained in well-known CoCrFeMnNi high entropy alloy.
- Rietveld refinement enabled to quantify the existing phases across the welded joints and establish microstructure/properties for the evaluated material systems.

CRediT authorship contribution statement

Jiajia Shen: Data curation, Formal analysis, Investigation, Writing – original draft. **Alexander C. Martin:** Data curation, Formal analysis, Investigation. **Norbert Schell:** Investigation. **Carolin Fink:** Investigation, Supervision, Funding acquisition, Methodology, Formal analysis, Writing – review & editing. **J.P. Oliveira:** Investigation, Supervision, Funding acquisition, Methodology, Formal analysis, Writing – review & editing.

Declaration of Competing Interest

The authors declare that they have no known competing financial interests or personal relationships that could have appeared to influence the work reported in this paper.

Data Availability

Data will be made available on request.

Acknowledgements

JPO and JS acknowledge Fundação para a Ciência e a Tecnologia

(FCT - MCTES) for its financial support via the project UID/00667/2020 (UNIDEMI). JS acknowledges the China Scholarship Council for funding the Ph.D. grant (CSC NO. 201808320394). JPO acknowledges funding by national funds from FCT - Fundação para a Ciência e a Tecnologia, I. P., in the scope of the projects LA/P/0037/2020, UIDP/50025/2020 and UIDB/50025/2020 of the Associate Laboratory Institute of Nanostructures, Nanomodelling and Nanofabrication – i3N. The authors acknowledge DESY (Hamburg, Germany), a member of the Helmholtz Association HGF, for the provision of experimental facilities. Beamtime was allocated for proposal I-20210899 EC. The research leading to this result has been supported by the project CALIPSOplus under the Grant Agreement 730872 from the EU Framework Programme for Research and Innovation HORIZON 2020. CF and ACM gratefully acknowledge partial financial support for this research by the Institute of Materials Research (IMR) at The Ohio State University under a 2017 Exploratory Materials Research Grant, and by the American Welding Society (AWS) under an AWS Graduate Research Fellowship Grant. Electron microscopy was performed at the Center for Electron Microscopy and Analysis (CEMAS) at The Ohio State University.

References

[1] B. Cantor, I.T.H. Chang, P. Knight, A.J.B. Vincent, Microstructural development in equiatomic multicomponent alloys, Mater. Sci. Eng.: A 375–377 (2004) 213–218, https://doi.org/10.1016/j.msea.2003.10.257.

[2] J.-W. Yeh, S.-K. Chen, S.-J. Lin, J.-Y. Gan, T. Chin, T.-T. Shun, C. Tsau, S.-Y. Chang, Nanostructured high-entropy alloys with multiple principal elements: novel alloy design concepts and outcomes, Adv. Eng. Mater. 6 (2004) 299–303, https://doi.org/10.1002/adem.200300567.

[3] N. Kashaev, V. Ventzke, N. Stepanov, D. Shaysultanov, V. Sanin, S. Zherebtsov, Laser beam welding of a CoCrFeNiMn-type high entropy alloy produced by self-propagating high-temperature synthesis, Intermetallics 96 (2018) 63–71, https://doi.org/10.1016/j.intermet.2018.02.014.

[4] J.G. Lopes, J.P. Oliveira, A short review on welding and joining of high entropy alloys, Metals 10 (2020) 212, https://doi.org/10.3390/met10020212.

[5] A.C. Martin, C. Fink, Initial weldability study on Al0.5CrCoCu0.1FeNi high-entropy alloy, Weld. World 63 (2019) 739–750, https://doi.org/10.1007/s40194-019-00702-7.

[6] H. Nam, S. Park, E.-J. Chun, H. Kim, Y. Na, N. Kang, Laser dissimilar weldability of cast and rolled CoCrFeMnNi high-entropy alloys for cryogenic applications, Sci. Technol. Weld. Join. 25 (2020) 127–134, https://doi.org/10.1080/13621718.2019.1644471.

[7] J.P. Oliveira, T.M. Curado, Z. Zeng, J.G. Lopes, E. Rossinyol, J.M. Park, N. Schell, F. M. Braz Fernandes, H.S. Kim, Gas tungsten arc welding of as-rolled CrMnFeCoNi high entropy alloy, Mater. Des. 189 (2020), 108505, https://doi.org/10.1016/j.matdes.2020.108505.

[8] Z. Wu, S.A. David, D.N. Leonard, Z. Feng, H. Bei, Microstructures and mechanical properties of a welded CoCrFeMnNi high-entropy alloy, Sci. Technol. Weld. Join. 23 (2018) 585–595, https://doi.org/10.1080/13621718.2018.1430114.

[9] P. Li, H. Sun, S. Wang, X. Hao, H. Dong, Rotary friction welding of AlCoCrFeNi2.1 eutectic high entropy alloy, J. Alloy. Compd. 814 (2020), 152322, https://doi.org/10.1016/j.jallcom.2019.152322.

[10] S. Park, H. Nam, Y. Na, H. Kim, Y. Moon, N. Kang, Effect of initial grain size on friction stir weldability for rolled and cast CoCrFeMnNi high-entropy alloys, Met. Mater. Int. 26 (2020) 641–649, https://doi.org/10.1007/s12540-019-00466-1.

[11] D. Shaysultanov, N. Stepanov, S. Malopheyev, I. Vysotskiy, V. Sanin, S. Mironov, R. Kaibyshev, G. Salishchev, S. Zherebtsov, Friction stir welding of a carbon-doped CoCrFeNiMn high-entropy alloy, Mater. Charact. 145 (2018) 353–361, https://doi.org/10.1016/j.matchar.2018.08.063.

[12] Z.G. Zhu, Y.F. Sun, F.L. Ng, M.H. Goh, P.K. Liaw, H. Fujii, Q.B. Nguyen, Y. Xu, C. H. Shek, S.M.L. Nai, J. Wei, Friction-stir welding of a ductile high entropy alloy: microstructural evolution and weld strength, Mater. Sci. Eng.: A 711 (2018) 524–532, https://doi.org/10.1016/j.msea.2017.11.058.

[13] S. Niu, H. Kou, T. Guo, Y. Zhang, J. Wang, J. Li, Strengthening of nanoprecipitations in an annealed Al0.5CoCrFeNi high entropy alloy, Mater. Sci. Eng.: A 671 (2016) 82–86, https://doi.org/10.1016/j.msea.2016.06.040.

[14] G. Vander Voort, E. Manilova, Metallographic techniques for superalloys, Microsc. Microanal. 10 (2004) 690–691, https://doi.org/10.1017/S1431927604883442.

[15] H.M. Daoud, A.M. Manzoni, N. Wanderka, U. Glatzel, High-temperature tensile strength of Al10Co25Cr8Fe15Ni36Ti6 compositionally complex alloy (high-entropy alloy), JOM 67 (2015) 2271–2277, https://doi.org/10.1007/s11837-015-1484-7.

[16] A.M. Manzoni, S. Haas, J.M. Yu, H.M. Daoud, U. Glatzel, H. Aboulfadl, F. Mücklich, R. Duran, G. Schmitz, D.M. Többens, S. Matsumura, F. Vogel, N. Wanderka, Evolution of γ/γ' phases, their misfit and volume fractions in Al10Co25Cr8Fe15Ni36Ti6 compositionally complex alloy, Mater. Charact. 154 (2019) 363–376, https://doi.org/10.1016/j.matchar.2019.06.009.

[17] A. Manzoni, S. Haas, H. Daoud, U. Glatzel, C. Förster, N. Wanderka, Tensile behavior and evolution of the phases in the Al10Co25Cr8Fe15Ni36Ti6 compositionally complex/high entropy alloy, Entropy 20 (2018) 646, https://doi.org/10.3390/e20090646.

[18] K. Prasad, M. Obana, A. Ito, S. Torizuka, Synchrotron diffraction characterization of dislocation density in additively manufactured IN 718 superalloy, Mater. Charact. 179 (2021), 111379, https://doi.org/10.1016/j.matchar.2021.111379.

[19] I. Moravcik, J. Cizek, P. Gavendova, S. Sheikh, S. Guo, I. Dlouhy, Effect of heat treatment on microstructure and mechanical properties of spark plasma sintered AlCoCrFeNiTi0.5 high entropy alloy, Mater. Lett. 174 (2016) 53–56, https://doi.org/10.1016/j.matlet.2016.03.077.

[20] X. Fu, C.A. Schuh, E.A. Olivetti, Materials selection considerations for high entropy alloys, Scr. Mater. 138 (2017) 145–150, https://doi.org/10.1016/j.scriptamat.2017.03.014.

[21] A.C. Martin, J.P. Oliveira, C. Fink, Elemental effects on weld cracking susceptibility in AlxCoCrCuyFeNi high-entropy alloy, Metall. Mater. Trans. A 51 (2020) 778–787, https://doi.org/10.1007/s11661-019-05564-8.

[22] S. Singh, N. Wanderka, B.S. Murty, U. Glatzel, J. Banhart, Decomposition in multi-component AlCoCrCuFeNi high-entropy alloy, Acta Mater. 59 (2011) 182–190, https://doi.org/10.1016/j.actamat.2010.09.023.

[23] Y. Yu, P. Shi, K. Feng, J. Liu, J. Cheng, Z. Qiao, J. Yang, J. Li, W. Liu, Effects of Ti and Cu on the microstructure evolution of AlCoCrFeNi high-entropy alloy during heat treatment, Acta Metall. Sin. (Engl. Lett.) 33 (2020) 1077–1090, https://doi.org/10.1007/s40195-020-01002-6.

[24] L. Moravcikova-Gouvea, I. Moravcik, M. Omasta, J. Veselý, J. Cizek, P. Minárik, J. Cupera, A. Záděra, V. Jan, I. Dlouhy, High-strength Al0.2Co1.5CrFeNi1.5Ti high-entropy alloy produced by powder metallurgy and casting: a comparison of microstructures, mechanical and tribological properties, Mater. Charact. 159 (2020), 110046, https://doi.org/10.1016/j.matchar.2019.110046.